1T-rich 2D-WS_2 as Interfacial Agent to Escalate Photo-induced Charge Transfer Dynamics in a Dopant-free Perovskite Solar Cells

Naveen Harindu Hemasiri, [a] Samrana Kazim, [a,b] and Shahzada Ahmad [a,b,*]

The rapid scientific surge in halide perovskite solar cells (PSCs) is owing to their solution processability and high power conversion efficiency, however, the deficiency in the photo-induced charge transfer dynamics at the perovskite-charge transport layer interfaces due to depleted energy alignment and surface traps impedes performance improvement. Interface engineering has become one of the rewarding approaches to control the charge accumulation and recombination at interfaces, which in turn promote excellent charge extractability and device performance. Here, we introduce a few atom thick 1T-rich 2D-WS_2 as an interfacial layer placed on perovskite to minimize energy barrier and charge accumulation at the interface to intensify extraction of detrapped charges and charge transfer dynamics. By combining the interfacial layer in a dopant free hole transport layer, we achieved a stabilized efficiency of over 19% with significantly enhanced open-circuit voltage and fill factor. Our work put forward the deep experimental understanding of 2D materials as an interfacial agent toward the stabilized performances.

Introduction

Among the next-generation photovoltaics (PV) technology, perovskite solar cells (PSCs) gave unparalleled power conversion efficiency (PCE) over 25%, which is on par with mature technology. The success of PSC is plagued by their frail stability under long-term operational conditions, which derails the commercialization of this promising technology[1-5]. In the perovskite-based PV, the synthetic pathways that include but are not limited to compositional engineering, temperature profile, and additive concentration largely influence the resulting PV performances and ultimately the device stability. Despite the astonishing compositional engineering that has been studied by many groups, challenges remain to achieve long-term stability that is heightened from ionic migration, light irradiation, moisture corrosion of the PSCs[6-7].

Beyond the active layer, the energy band alignment of the perovskite layer at the interfaces with the charge selective layers is a prerequisite in governing device performance and stability[4,8,9]. Perovskites are sandwich between charge selective layers with possibly associated energy and chemical incompatibilities with the contacting layers making the interfaces a crucial zone with high potential to instigate device failure[4,6,10,11]. Arguably, photo-generated charge separation and transfer to the corresponding interfaces from the light-absorbing layer could occur with the absence of energy losses without recombination at the interfaces. Moreover, the ideal electron/hole selective layers should allow their corresponding charges only, while making no recombination and transport losses at the interfaces[10,12,13]. However, due to imbalance charge separation and transfer, inferior interface band alignment, defects associated with the interfaces under real conditions can deteriorate the PV performances of PSCs[12,14-16].

At the device level, stress due to extrinsic environmental conditions such as varying temperature, electric field, atmosphere, and light intensity intensively propagate degradation mechanism[17,18]. Furthermore, unbalanced charge injection, trapped charges, and capacitive current promote the charge accumulation at the interfaces between perovskite and charge selective layers, and ultimately the trapped charged-driven degradation may take place in addition to the photo-generated hysteresis[19-21].

Several approaches have been devoted toward the long term PV performance including an introduction of interface energy alignment layer, tuning the work function of perovskite layer, doping mechanism into charge transport layers, and self-assembled derivatives to overcome photo-generated carrier traps, improving the quality of the interfacial coupling, and defect passivation[4,8,9]. However, the hygroscopic nature associated with doping or interfacial materials can further accelerate the degradation of the perovskite layer[22-24]. The accession of the interfacial layer gave promising results in terms of PV performances and stability[26-29]. The analog of 2D materials termed as 2D transition metal dichalcogenides (TMDs) is a promising class of semiconductors for PV applications including PSCs due to their outstanding chemical, physical and electronic properties which can be further tuned by synthesis route[7,29,30]. However, scalable synthesis of 2D-TMD materials with high purity and specific functionalities remains a key to advanced PV applications. Among different synthetic protocols, Li^+ intercalated liquid-phase exfoliation of layered materials is a promising approach that offers high yield, simplistic method, up-scalability, and cost-effectiveness. Reports dealing with 2D-TMDs such as MoS_2 and WS_2 in PSCs as HTM gave moderate PCE values[31]. Several groups have investigated the behaviour of 2D-MoS_2 and WS_2 as electron transport layers (ETM) in PSCs[2,32,33]. However, the PCE associated with 2D-TMDs as an individual HTM or ETM is not comparable towards the commercialization, stipulating the limitation of 2D-TMDs as individual charge transport layers. In contrast, the utilization of 2D-TMDs as an interfacial layer between the active and charge transport layer gave significantly improved PV performance with an extended lifetime[7,23,34-36]. Owing to non-covalent interaction and the dangling-bonds-free nature of 2D-TMDs could further stabilize the active layer from hygroscopic additives in charge transport

[a] BCMaterials, Basque Center for Materials, Applications and Nanostructures, UPV/EHU Science Park, 48940, Leioa, Spain
Email: shahzada.ahmad@bcmaterials.net
[b] IKERBASQUE, Basque Foundation for Science, Bilbao, 48009, Spain

materials[29,35]. Earlier, we have reported, Li^+ intercalated 2D-MoS_2 as an interfacial layer in dopant-free *n-i-p* PSCs, achieving upgraded PCE.

Herein, we report our findings of successfully implemented Li^+ intercalated liquid-phase exfoliated 2D-WS_2 as an interfacial layer on a triple cation $\{Cs_{0.1}FAPbI_{3(0.81)}MAPbBr_{3(0.09)}\}$ perovskite (CsFAMA), leading to significantly enhanced PCE and an expanded lifetime. We noted that the 2D-WS_2 as an interlayer could diminish the surface traps and interfacial charge recombination at perovskite/HTM interface through the aligned energy level, subsequently boosting the PCE from 15.7% to 19.02% owing to boosted open-circuit voltage (V_{oc}) and fill factor (FF).

Result and Discussions

We derived few layers of 1T predominant WS_2 nanosheets in isopropanol (IPA) from bulk WS_2 powder using rapid Li^+ intercalation in combination with ultra-sonication and a series of ultracentrifugation steps. During the Li^+ intercalation process into WS_2, the lithiation intermediate (Li_xWS_2) was thoroughly reacted with H_2O to separate the van der Waals bonded layers and form a few or single-layer WS_2 sheets. The microstructure of the synthesized 2D-WS_2 nanosheets was analysed under transmission electron microscopy (TEM) and atomic force microscopy (AFM) instruments. Figure 1a illustrates a representative TEM image of 2D-WS_2 with a lateral size of *c.a.*120 nm. The topographic AFM image (Figure 1b) together with the inset thickness profile suggests the thickness of the 2D-WS_2 in the 5-6 nm range, affirming the existence of a few-layer of nanosheets. Figure 1c shows the statistical distribution with the maximum population peaks at 5.15 nm. The X-ray diffraction (XRD) pattern of 2D-WS_2 shows a high intense single diffraction peak at 2θ of 14.52°, corresponding to the (002) crystal plane of hexagonal WS_2, and absence of additional peaks from bulk WS_2, confirming the highly oriented phase crystallinity of the synthesized 2D-WS_2 nanosheets[2] (Figure S1). The UV-Vis absorption of 2D-WS_2 nanosheets dispersed in IPA solution (Figure 1d), exhibit the weak shoulder peaks located at 637 and 528 nm corresponds to the A and B excitonic transitions, confirm the formation of 1T rich 2D-WS_2 nanosheets[37]. The optical bandgap estimated from the Tauc plot is about 1.76 eV (inset of Figure 1d).

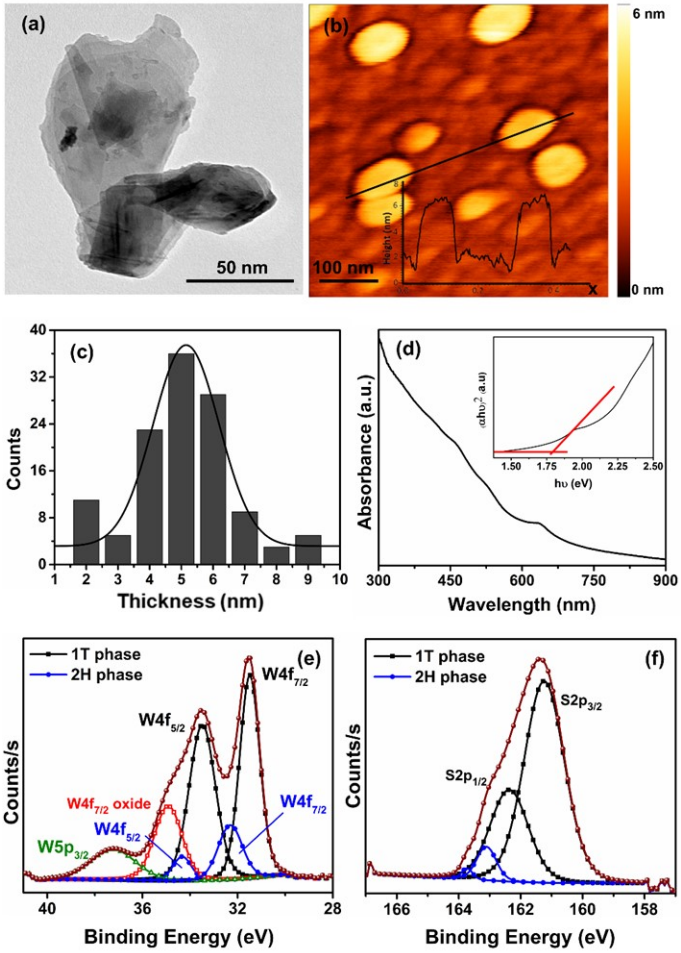

Figure 1. Characterization of the synthesized 2D-WS_2. (a) TEM image of WS_2 flakes, (b) AFM image of selected WS_2 flakes. Inset represents thickness profile of the selected flakes, (c) statistical distribution of WS_2 flakes thickness, (d) optical absorption spectrum. Inset: calculated optical band gap of WS_2 flakes from the Tauc plot. High-resolution XPS of (e) W4f spectra and (f) S2p spectra.

The positions of core-level peaks corresponding to $W4f_{7/2}$ and $W4f_{5/2}$ originated from X-ray photoelectron spectroscopy (XPS) is an effective way to specify the phase and chemical state of the elements composing the 2D-WS_2 nanosheets. We ascribed the emerged doublet (Figure 1e) at 31.49 and 33.48 eV to the $W4f_{7/2}$ and $W4f_{5/2}$ core levels of metallic 1T phase respectively, attributing the presence of predominant contribution of 1T phase with 82.25% in the as-prepared 2D-WS_2. However, the less intense additional peaks at 32.31 and 34.33 eV was also observed, showing the simultaneous existence of partial semiconducting 2H phase in WS_2 nanosheet[37]. Similar phase contribution can be deduced from high-resolution XPS of S2p (Figure 1f), in which two identical peaks relevant to $S2p_{3/2}$ and $S2p_{1/2}$ for 1T phase emerged at 161.24 and 162.37 eV respectively.

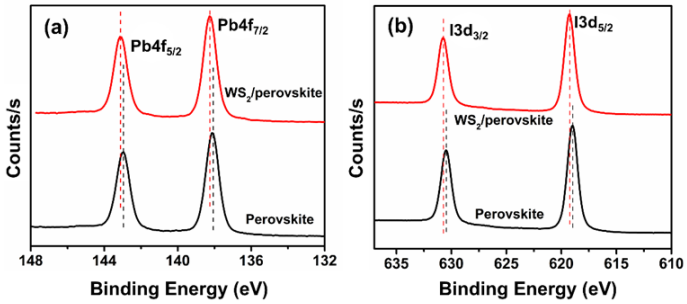

Figure 2. High-resolution XPS of (a) Pb4f and (b) I3d for perovskite and perovskite/2D-WS_2 films.

We examined the microstructure of the CsFAMA perovskite layer grown on the SnO_2 QDs layer using SEM and AFM analysis (Figure S2). Notably from AFM analysis, we deduce that the perovskite roughness decreases from 21.48 nm to 16.16 nm after the deposition of 2D-WS_2 nanosheets on perovskite. However, full coverage of the 2D-WS_2 layer on perovskite can only be achieved through multiple depositions of the solution of 2D-WS_2 as previously reported, in this report, we deposited three times 2D-WS_2 nanosheets.

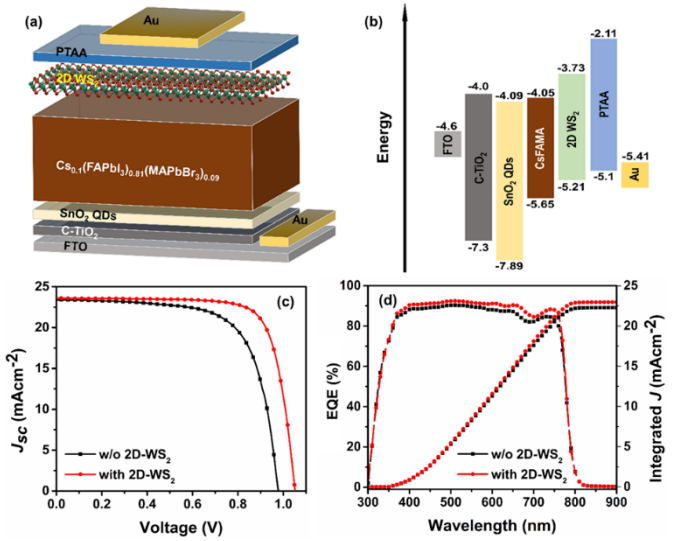

Figure 3. (a) Device structure of planar perovskite solar cells incorporating 2D WS_2 interface layer, (b) energy band alignment of the corresponding layers, (c) *J-V* curves of the devices with and without interface layer, and (d) corresponding EQE and integrated current of the devices.

The XRD analysis (Figure S3) indicates the presence of 2D-WS_2 does not influence the crystallinity of the perovskite. The interaction between 2D-WS_2 nanosheets and the perovskite layer at the interface was further investigated using XPS characterization. As shown in Figure 2a the $Pb4f_{5/2}$ and $Pb4f_{7/2}$ peaks of the bare perovskite layers located at 142.98 and 138.1 eV respectively, these peaks show an apparent binding energy shift of 0.11 eV towards the higher binding region with the presence of 2D-WS_2 layer. A similar binding energy shift can be deduced in I3d peaks when the perovskite layer is placed with 2D-WS_2 in which the shift is around 0.15 eV (Figure 2b), corroborating a possible strong interaction of S-Pb, S-I, and modified chemical environment of $[PbI_6]^{4-}$ octahedral[34,38,39]. No visible changes were noted in the UV-visible spectra of the perovskite with/without the 2D WS_2 interface layer (Figure S4). PSCs were fabricated based on planer *n-i-p* configuration with stacked layers of FTO/bl-TiO_2/SnO_2-QDs/$Cs_{0.1}FAPbI_{3(0.81)}MAPbBr_{3(0.09)}$/2D-$WS_2$/PTAA/Au (Figure 3a) to evaluate the PV performances by the placement of 2D-WS_2 as an interfacial layer. The energy levels of the materials used in the device architect including as prepared 2D-WS_2 (Figure 3b) suggest the compatibility of the valence band energy of the interface layer at HTM/perovskite interface which overcomes the energy barrier for effective free hole extraction[6,40-43]. SnO_2 layer together with thin compact-TiO_2 acts as electron selective contact to prevent direct contact to the bottom charge collector, annihilating a possible charge recombination path. We acquired the cross-section image of fabricated PSC by scanning electron microscopy (SEM) (Figure S5).

Table 1. Photovoltaic parameters of the champion devices with or without 2D-WS_2 interface layer.

Device	Scan	V_{oc} (mV)	J_{sc} (mAcm^{-2})	FF (%)	PCE (%)	R_s (Ω)	R_{sh} (kΩ)	HI
With WS_2 (hero)	RS	1051.6	23.59	76.68	19.02	36.54	61.12	0.02
	FS	1041.6	23.24	76.93	18.62	38.77	45.27	
With WS_2 (avg.)	RS	1043.12 ± 10.15	23.31 ± 0.39	76.86 ± 0.68	18.69 ± 0.31			
Without WS_2 (hero)	RS	976.7	23.39	68.88	15.74	46.75	19.52	0.05
	FS	967.6	23.29	66.47	14.98	52.33	14.38	
Without WS_2 (avg.)	RS	970.90 ± 9.89	22.66 ± 0.86	70.01 ± 2.41	15.38 ± 0.36			

The photocurrent-density-voltage (*J-V*) characteristics of PSCs with and without interface layer are illustrated (Figure 3c), and the corresponding PV parameters are summarized in Table 1. A significant increase was measured from the PSCs incorporating 2D-WS_2 as an interlayer, and a value of 19.02% PCE with an open-circuit voltage (V_{oc}) of 1051 mV, a short-circuit current density (J_{sc}) of 23.59 mAcm^{-2}, and a fill factor (FF) of 76.68%. Under a similar condition, control devices showed PCE of 15.74% with V_{oc}, J_{sc}, and FF as 976.7 mV, 23.39 mAcm^{-2}, and 68.88% respectively. Notably, the PSCs with an interface layer show an average improvement of PCE by 23.5% from the control PSC owing to an improvement in V_{oc} and FF. The integrated J_{sc} values extracted from external quantum efficiency (EQE) measurement are 22.97 and 22.28 mAcm^{-2} for the PSC with and without the interface layer, in agreement with the J_{sc} obtained from *J-V* curves (Figure 3d). The corresponding integrated currents of the two PSCs show a slight reduction compared to the J_{sc} obtained from the *J-V* curve possibly due to the difference in the light source used, which is much lower in intensity than of the solar simulator system[29]. Notably, we noted a significant drop in device hysteresis after introducing the interface layer (Figure 4a). We attribute the enhanced V_{oc} to the reduction of the high energy barrier between the valence

band energy level of perovskite (E_V = -5.65 eV) and HOMO level of PTAA (-5.1eV) by placing the interface layer, this facilitates a facial photo-generated charge transfer between the perovskite and PTAA layer[7,23]. Moreover, the PSC fabricated with the 2D-WS_2 interfacial layer shows decreased interfacial series resistance (R_s) and higher shunt resistance (R_{sh}) which suppresses interfacial charge losses through decreased charge recombination, to push the FF.

The influence of the 2D-WS_2 interface layer on charge dynamics in the PSCs was analyzed using electrochemical impedance spectroscopy (EIS) under dark conditions. The Nyquist plot with the equivalent circuit model (Figure 4b, and Table S3) that comprises single series resistance (R_s), charge transfer resistance (R_{ctr}), charge recombination resistance (R_{rec}) at the interface between perovskite/HTL, and two constant phase elements related to carrier diffusion in perovskite and selective layers (CPE1 and CPE2). We noted that at a given potential bias, the R_{ctr} in the PSC with 2D-WS_2 interfacial layer is much lower than that of the control device, inferring that the interfacial layer imparts a critical role in promoting the charge transfer dynamics at the perovskite/HTM interface (Figure 4c). The relative trend of R_{ctr} is in agreement with the R_s obtained from the *J-V* curves. This reduced R_s correlated with the lower R_{ctr} further confers the enhanced FF of the device with the 2D-WS_2 interfacial layer[44]. Further, at a similar potential bias, the PSC with the interfacial layer features a higher R_{rec} than the control device, which reflects the higher resistance for charge annihilating at the interface (Figure 4d). The carrier recombination behaviour was further assessed by the semi-logarithmic *J-V* curve in the dark (Figure 4e). By fitting the exponential region of the curve with the Shockley equation that is given by[45-46],

$$J_{dark} = J_0\left[exp\left(\frac{V}{n_{id}K_BT}\right) - 1\right],$$

in which J_{dark}, is the dark current density, J_0 is the saturation current density, V is the applied voltage, q is the electron charge, K_B is the Boltzmann constant, T is the temperature, and n_{id} is the ideality factor. We estimated the J_0 and n_{id} for the control PSC to be 4.834 × 10^{-6} $mAcm^{-2}$ and 2.69 respectively, whereas, the device with the 2D-WS_2 interface layer is 2.109 ×10^{-7} $mAcm^{-2}$ and 2.47 respectively. Such low J_0 and n_{id} values associated with the 2D-WS_2 interface layer usage indicates a low leakage current density and significantly hindered carrier recombination, enhancing the charge transfer dynamics in the PSC. This escalates the FF, V_{oc}, and subsequently the PCE of the PSC with the use of interfacial layer[30,47]. The dark current results are consistent with the R_{rec} obtained from the EIS measurements.

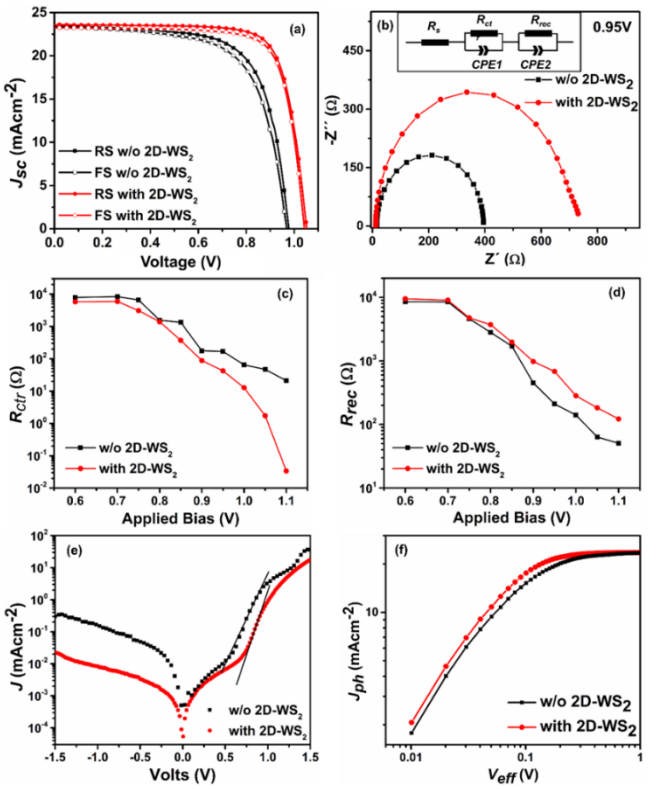

Figure 4: (a) *J-V* hysteresis curve of forward and reverse scan of the PSCs, (b) electrochemical impedance spectra measured under an applied voltage of 0.95 V in a dark condition of PSCs. The inset is the equivalent circuit used for the fitting of impedance spectra. The potential bias-dependent (c) charge transport resistance and (d) interfacial charge recombination resistance, (e) dark *J-V* curve of the PSCs, and (f) photo-generated current density, J_{ph} vs. effective voltage (V_{eff}).

To identify the charge collection and exciton dissociation in the presence of the 2D-WS_2 interlayer, we measure (Figure 4f) the photocurrent density (J_{ph}) as a function of effective voltage (V_{eff}). The J_{ph} is defined as the difference between the current density under illumination (J_L) and dark (J_D); (J_{ph} = J_L- J_D). The term V_{eff} follows the formula of V_{eff} = V_0 − V, where V_0 is the compensation voltage defined as J_{ph} = 0, and V is the applied voltage[47-49]. Remarkably, the device with the 2D-WS_2 interface layer displays a saturation of photocurrent at a relatively low V_{eff} (0.3 V) compared to that of the control PSC (0.58 V), suggesting an effective charge extraction behaviour in the PSC with a 2D-WS_2 interfacial layer. Ideally, the efficiency of charge dissociation and collection depends on the maximum exciton generation rate (G_{max}), which follows the relation of J_{sat} = eLG_{max}, where J_{sat}, e, and L are saturated J_{ph}, elementary charge, and the thickness of the perovskite layer respectively[49]. As tabulated (Table S4), we calculated the G_{max} to be 3.68 × 10^{21}/s for the 2D-WS_2 interface-layer-based PSC that is slightly higher than 3.65 × 10^{21}/s for the control PSC. This enhanced G_{max} suggests that the introduction of a 2D-WS_2 layer at the PTAA/perovskite interface promotes the interfacial charge transfer dynamics in the PSCs.

Arguably, photo-generated charge carriers can easily drift under an operational electric field and accumulate at the interfaces due to poor band alignment and/or poor mobility of the charge transport layers or poor charge extraction, which promotes the

charge build-up at the interface and consequently deficit the V_{oc}[50-52]. Additionally, the trap density plays a foremost role in governing the overall performance of the PSC in which the trapped charges at the interface show restriction to their mobility. The increase in trap density can further diminish the trapped charge carriers through nonradiative recombination, limiting the PCE[51]. To gain further insight into charge accumulation behaviour at the perovskite/HTL interface with and without the 2D-WS_2 interface layer, we performed the temperature-dependent capacitance-frequency (*c-f*) measurement.

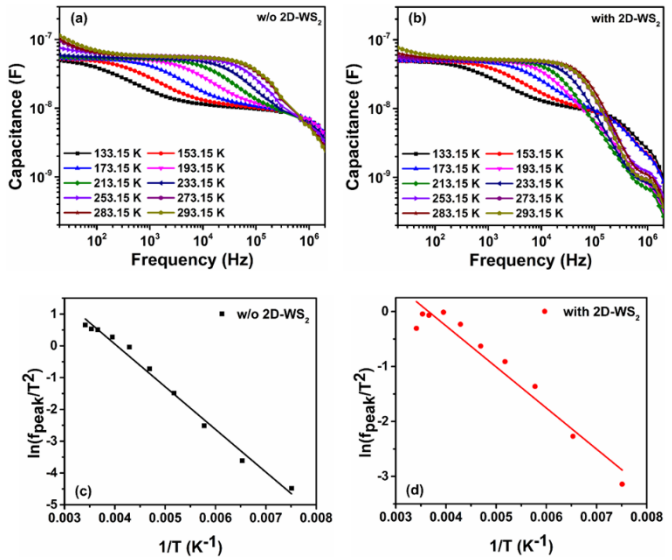

Figure 5. Temperature-dependent capacitance-frequency (*c-f*) measurements of the devices without (a) and with (b) 2D-WS_2 interfacial layer, Arrhenius plot of the devices without (c) and with (d) 2D-WS_2 interfacial layer.

Figure 5 a and b show *c-f* data for PSCs as a function of temperature from 133.15 – 293.15K under short circuit dark conditions. We noted that below 213.15K, geometrical capacitance, as determined from the constant capacitance plateau at the intermediate frequency region, freeze-out in both devices. Deeper traps participate in capacitance as the frequency decreases resulting in a capacitance build-up at the low-frequency region[53]. In the low-frequency region, the control device shows limited capacitance build-up from low temperature until 233.15K, and later, thermally-activated capacitance shows a significant increment that can be ascribed to the charge accumulation and build-up at the interfaces[53,54]. In particular, the PSC with the additional interfacial layer display nearly constant capacitance until 253.15K from low temperature throughout the low-frequency region, and then it increases slightly, beyond this temperature. However, the capacitance build-up is high in the PSCs without the interfacial layer as compared to the PSC with the 2D-WS_2 layer, confirming that the 2D-WS_2 layer can hinder the charge accumulation at the perovskite/PTAA interface. Figure S6 further illustrates the temperature-dependent capacitance variation in the PSC at low frequency (10^2 Hz). We investigated the trap profile associated with the PSCs by identifying the characteristic trap emission parameter, known as an attempt to escape frequency (v_0), which represents the dynamics of trap emission and defines the maximum rate of detrapping the trapped charges. Figures 5 c and d illustrate the variation of the frequency of peak emission rate (f_{peak}) of charges from trap state with the temperature, in which the f_{peak} increases gradually with temperature from 133.15K until room temperature and then plateau on a further increment of temperature (Figure S7). According to the Arrhenius relationship, the emission rate (e_n) of trapped charge in a defect shows the following correlation with the associated trap activation energy E_T[54],

$$\ln\left(\frac{e_n}{T^2}\right) = \ln\left(\frac{v_0}{T^2}\right) - \frac{E_T}{K_b T}$$

where e_n being the measurement frequency at peak (f_{peak}), K_b is the Boltzmann constant, and T is the temperature. The calculated trap energy for the PSC with and without 2D-WS_2 is 115.63 and 64.38 meV respectively from the trap energy plot (Figure 5 c and d). The corresponding v_0 of the control PSC is 2.04×10^7 Hz that is much higher than that of the PSC with the interface layer (1.38×10^6 Hz).

We identified the trap-state distributions and energies affected by the 2D-WS_2 interface layer, by the trap state profile using thermal admittance spectroscopy along with the Mott-Schottky spectra (Figure 6a). At room temperature, the built-in-potential (V_{bi}) and the depletion layer thickness (w) obtained for the control PSC are 991.80 mV and 140.17 nm, respectively; expectedly, the PSC with 2D-WS_2 interface layer shows improved results achieving V_{bi} of 1073.85 mV and w of 236.10 nm. The increased V_{bi} and w escalates the charge separation and transfer at the perovskite/PTAA interface. The trap density profiles (Figure 6b) at room temperature (303.15 K), for control PSC, a peak trap density of 3.45×10^{17} $cm^{-3}eV^{-1}$ at 0.134 eV appears. While the PSC with 2D-WS_2 displays a smaller peak intensity of 2.58×10^{17} $cm^{-3}eV^{-1}$ at a shallow energy level of 0.77 eV. Further, the control PSC shows an intense trap density across the higher energy region from 0.3 – 0.36 eV. Based on these results, we can conclude that the 2D-WS_2 interface layer can passivate charge traps at the perovskite interface. This highlights the critical role of the interface layer in controlling the interface charge separation and recombination in the device, leading to a significant improvement in V_{oc} and PCE.

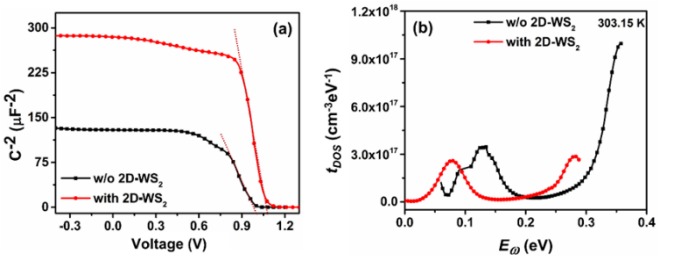

Figure 6. (a) Mott-Schottky analysis at 10 kHz and (b) trap density of states deduced from temperature-dependent *c-f* spectroscopy for the devices without and with 2D-WS_2.

The beneficial role played by the incorporation of the 2D-WS_2 layer on charge transfer dynamics while promoting PV performances, led us to study its impact on the long-term operational stability, MPP tracking[55] of un-encapsulated PSCs was conducted under 1 sun illumination at room temperature with 50-60 % humidity (Figure 7). The control PSC reached 80%

of its initial photocurrent after 8 h of continuous illumination and photocurrent reduces continuously under ambient conditions, while, under similar conditions, the PSC with the 2D-WS_2 interface layer retained 80% of its initial photocurrent for 100 h. Moreover, the PSC with a 2D-WS2 interfacial layer showed more stabilized J_{sc} and V_{oc} (Figure 7 b and c). 2D-WS_2 deposited on the perovskite layer yielded a higher contact angle of 87±10 compared to that of bare perovskite (81±10) suggesting, the hydrophobic nature associated with the 2D-WS_2 that can mitigate the water penetration into the active perovskite layer in the PSC (Figure S8).

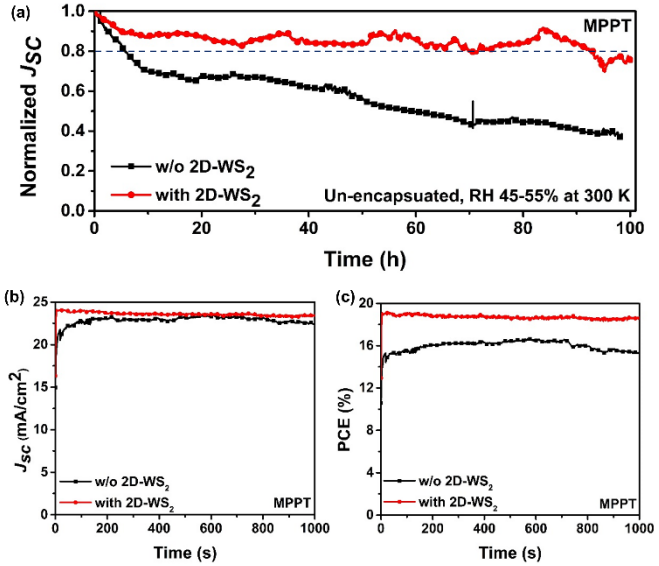

Figure 7. (a) Normalized Jsc for 100 h of continuous MPP tracking for unencapsulated devices under constant ambient atmosphere. Initial 1000 s MPP tracking of (b) J_{sc} and (c) V_{oc}.

Conclusions

In summary, we demonstrated the role of 1T-rich 2D-WS_2 nanosheets, particularly synthesized via Li^+ intercalated liquid-phase exfoliation, in enhancing optoelectronic properties via stimulating the photo-induced charge transfer dynamics and suppressing the surface trap density. We found that the trap density in the device decreased by 25% with a saturation of photocurrent at a relatively low V_{eff} (0.3V) due to the 2D-WS_2 interfacial layer. The presented protocol based on the introduction of 2D-WS_2 between the un-doped PTAA and the perovskite absorber enabled to demonstrate *n-i-p* PSCs with a stabilized efficiency of over 19%, paving the way toward reliability enhancement in PSCs for commercial viability.

Experimental

Materials:

Lead Iodide (99.9%) was purchased from Tokyo Chemical Industry (TCI) and employed as such. Methylammonium iodide (MAI) and formamidinium iodide (FAI) was purchased from Dyesol. Solvents mainly DMF, DMSO, Ethyl acetate, Ethanol, Chlorobenzene were purchased from Acros Chemicals and used as such.

Synthesis of 2D WS_2

We performed the intercalation of WS_2 according to the previous report[6,54]. Briefly, 50 mg of bulk WS_2 in 5 ml of butyl lithium/hexane solution was magnetically stirred for 48 h and then ultra-sonicated for 6 h. The resultant solution was left to stabilize and the upper solution was discarded. Excess butyl lithium was washed out by dilution with hexane and the residual was dispersed in isopropanol (IPA) and ultra-sonicated for 2 h. We centrifuged the resultant solution at 8000 rpm for 30 min, to remove the supernatant, and repeated the process. The residual was dispersed in IPA and centrifuged at 2000 rpm for 20 min and collected the 80% of upper supernatant for device fabrication.

Device Fabrication

We started by cleaning the laser-etched FTO-coated glasses (NSG10), with Hellmanex II solution, deionized water, acetone, and IPA under ultrasonication in the order. We then dried the substrates with compressed air and treated them with UV-ozone for 30 min before use. A compact blocking layer of TiO_2 was deposited onto FTO substrates by spray pyrolysis at 500 ºC employing 1/19mL of titanium (IV) diisopropoxide bis(acetylacetonate) precursor solution (75 % in 2-propanol) in pure ethanol keeping them for another 30 min. After the films acquired room temperature, the electrodes were subject to UV-ozone treatment for another 15 min. The synthesized SnO_2-QD solution was spin-coated atop of the compact layer at 500 rpm for 5 s and 5000 rpm for 35 s followed by annealing on a hot plate progressively at 200 ^oC for 1 h in air. Once cooled down to room temperature the samples were transferred to the Argon-filled glovebox (H_2O level: <1 ppm and O_2 level: <10 ppm). Triple-cation perovskite layers were deposited by spin coating the perovskite precursor solution containing CsI (0.10 M), FAI (1.05 M), PbI_2 (1.24 M), MABr (0.12M), and $PbBr_2$ (0.12 M) in an anhydrous solvent mixture of *N,N*-dimethylformamide (DMF) and dimethylsulfoxide (DMSO) with 4:1 volume ratio. The perovskite precursor solution was spin-coated on the as-prepared SnO_2-QD as ETL in a two-step spin-coating program set at 1000 rpm and 6000 rpm for 10 and 30 s. During the spin coating process, we slowly dripped 112 µL of chlorobenzene on the rotating substrate in the last 10 s before the termination of the program[54]. The deposited perovskite was annealed at 100 ^oC for 1 h to induce crystallization. After cooling down to room temperature 2D-WS_2 in isopropanol solution was spin-coated at 1000 rpm for 20 s and dried at 60 ^oC for 3 min (this was repeated three times to achieve a continuous layer with an average thickness of 9 nm). Pristine PTAA (10 mg/ml in toluene) was spin-coated at 3000 rpm for 35 s. For control PSCs, we deposited PTAA directly on the perovskite active layer. The photovoltaic devices were completed through evaporating Au (80 nm, <1 Å/s) in an evaporator with vacuum conditions below 10^{-7} Torr.

Device characterization

Current density-voltage (*J-V*) curves were performed using a 3A Oriel solar simulator (Newport) producing 1 sun AM1.5G (1000 Wm^{-2}). The generated photocurrent was recorded at a scan rate of 100 mV/s (pre-sweep delay: 10s) with the help of Keithley 2604 source meter. The active area of the device was 0.09 cm^{-2}. We measure the IPCE using a 150 W xenon lamp attached to a Bentham PVE300 motorized 1/4m monochromator.

Trap density measurements: Temperature-dependent capacitance-frequency measurements were performed with LCR meter model No. E4980A along with a Linkam (LTS420) sample heating control system filled with nitrogen in a closed environment. The energetic profile of trap density of state (t_{DOS}) was calculated with the following equations[56,57]:

$$N_T(E_\omega) = -\frac{v_{bi}}{qw}\frac{dC}{d\omega}\frac{\omega}{K_bT}$$

$$E_\omega = K_bTln\left(\frac{v_0}{\omega}\right)$$

$$\frac{1}{C^2} = \frac{2}{\varepsilon\varepsilon_0A^2qN}\left[v - v_{bi} - \frac{K_bT}{q}\right]$$

where V_{bi} is built-in-potential, w is depletion layer thickness, C is the capacitance measured at an angular frequency ω, T is temperature, K_b is Boltzmann constant, q is the elementary charge, ε is the relative dielectric constant of perovskite (c as 13 from a previous report)[57], ε_0 is the permittivity of free space and A is active interfacial area.

Materials and Thin-film Characterization

X-ray photoelectron spectroscopy (XPS) experiment was carried out on a SPECS system (Berlin, Germany) equipped with Phoibos 150 1D-DLD analyzer with monochromated Al K_α radiation (1486.7 eV). The wide scan was performed with the step energy of 1 eV (dwell time: 0.1 s, pass energy: 80 eV), and detailed analysis of the elements was performed using 0.08 eV step energy (dwell time: 0.1 s, pass energy: 30 eV) with an electron exit angle of 90°. The spectra were adjusted using CasaXPS 2.3.16 software, which models Gauss-Lorentzian contributions. X-ray diffractograms were recorded using a D8 Advance diffractometer from Bruker (Bragg-Brentano geometry, with an X-ray tube Cu Kα, λ=1.5406 Å). For surface topology and phase image, Atomic Force Microscopy (CSI Nano observer AFM) was used and data were analyzed using Gwyddion software. We registered the absorption spectra with the help of a UV–vis–IR spectrophotometer (Varian Cary 50 UV/Vis Spectrophotometer). The cross-section and top-view microstructure was acquired with the help of a Hitachi S-4800 scanning electron microscope.

Author Contributions

N.H.H performed the experiments, analysed the data, and prepared the initial draft, S.K. performed the electro-optical measurements, analysis of the data, conceived the idea, and S.A. supervised & directed the research. All authors contributed to the draft and prepared the final version.

Conflicts of interest

The authors declare no conflict of interest.

Acknowledgments

This work received funding from the European Union H2020 Programme under a European Research Council Consolidator grant [MOLEMAT, 726360]. PARASOL (RTI2018-102292-B-100), the Spanish Ministry of Science and Innovation. We thank SGiKER, UPV-EHU for the XPS analysis.

Notes and references

1 https://www.nrel.gov/pv/cell-efficiency.html, **n.d.**
2 N. A. A. Malek, N. Alias, A. A. Umar, X. Zhang, X. Li, S. K. M. Saad, N. A. Abdullah, H. Zhang, Z. Weng, Z. Shi, C. Li, M. M. Rosli, and Y. Zhan, *Sol. RRL*, 2020, **4**, 2000260.
3 L. T. Schelhas, Z. Li, J. A. Christians, A. Goyal, P. Kairys, S. P. Harvey, D. H. Kim, K. H. Stone, J. M. Luther, K. Zhu, V. Stevanovic, and J. J. Berry, *Energy Environ. Sci.*, 2019, **12**, 1341–1348.
4 L. Canil, T. Cramer, B. Fraboni, D. Ricciarelli, D. Meggiolaro, A. Singh, M. Liu, M. Rusu, C. M. Wolff, N. Phung, Q. Wang, D. Neher, T. Unold, P. Vivo, A. Gagliardi, F. De Angelis, and A. Abate, *Energy Environ. Sci.*, 2021, **14**, 1429–1438.
G. Zheng, C. Zhu, J. Ma, X. Zhang, G. Tang, R. Li, Y. Chen, L. Li, J. Hu, J. Hong, Q. Chen, X. Gao, and H. Zhou, *Nat. Commun.*, 2018, **9**.
5 C. Li, Z. Song, D. Zhao, C. Xiao, B. Subedi, N. Shrestha, M. M. Junda, C. Wang, C. -S. Jiang, M. Al-Jassim, R. J. Ellingson, N. J. Podraza, K. Zhu, and Y. Yan, *Adv. Energy Mater.*, 2018, **9**, 1803135.
6 X. Liu, Y. Cheng, B. Tang, Z. G. Yu, M. Li, F. Lin, S. Zhang, Y. -W. Zhang, J. Ouyang, and H. Gong, *Nano Energy*, 2020, **71**, 104556.
7 K. -G. Lim, S. Ahn, and T. -W. Lee, *J. Mater. Chem. C*, 2018, **6**, 2915–2924.
8 A. Agresti, A. Pazniak, S. Pescetelli, A. Di Vito, D. Rossi, A. Pecchia, M. A. der Maur, A. Liedl, R. Larciprete, D. V. Kuznetsov, D. Saranin, and A. Di Carlo, *Nat. Mater.*, 2019, **18**, 1264.
9 A. Rajagopal, K. Yao, and A. K. -Y. Jen, *Adv. Mater.*, 2018, **30**, 1800455.
10 T. Wang, Z. Cheng, Y. Zhou, H. Liu, and W. Shen, *J. Mater. Chem. A*, 2019, **7**, 21730–21739.
11 L. Calió, S. Kazim, M. Grätzel and S. Ahmad, *Angew. Chem. Int. Ed.*, 2016, **55**, 14522-14545.
12 N. E. Courtier, J. M. Cave, J. M. Foster, A. B. Walker, and G. Richardson, *Energy Environ. Sci*, 2019, **12**, 396–409.
13 S. Wang, T. Sakurai, W. Wen, and Y. Qi, *Mater. Interfaces*, 2018, **5**, 1800260.
14 M. I. Saidaminov, J. Kim, A. Jain, R. Quintero-Bermudez, H. Tan, G. Long, F. Tan, A. Johnston, Y. Zhao, O. Voznyy, and E. H. Sargent, *Nat. Energy*, 2018, **3**, 648–654.
15 I. Lee, J. H. Yun, H. J. Son, and T. -S. Kim, *ACS Appl. Mater. Interfaces*, 2017, **9**, 7029–7035.
16 K. Domanski, E. A. Alharbi, A. Hagfeldt, M. Grätzel, and W. Tress, *Nat. Energy*, 2018, **3**, 61–67.
17 A. R. Bowring, L. Bertoluzzi, B. C. O'Regan, and M. D. McGehee, *Adv. Energy Mater.*, 2017, **8**, 1702365.
18 N. Ahn, K. Kwak, M. S. Jang, H. Yoon, B. Y. Lee, J. -K. Lee, P. V. Pikhitsa, J. Byun, and M. Choi, *Nat. Commun.*, 2016, **7**.
19 B. Chen, M. Yang, S. Priya, and K. Zhu, *J. Phys. Chem. Lett.*, 2016, **7**, 905–917.
20 W. Tress, N. Marinova, T. Moehl, S. M. Zakeeruddin, M. K. Nazeeruddin, and M. Grätzel, *Energy Environ. Sci*, 2015, **8**, 995–1004.

21 L. -L. Jiang, Z. -K. Wang, M. Li, C. -H. Li, P. -F. Fang, and L. -S. Liao, *J. Mater. Chem. A*, 2019, **7**, 3655–3663.
22 G. Kakavelakis, I. Paradisanos, B. Paci, A. Generosi, M. Papachatzakis, T. Maksudov, L. Najafi, A. E. Del Rio Castillo, G. Kioseoglou, E. Stratakis, F. Bonaccorso, and E. Kymakis, *Adv. Energy Mater*., 2018, **8**, 1702287.
23 S. Tsarev, I. K. Yakushchenko, S. Y. Luchkin, P. M. Kuznetsov, R. S. Timerbulatov, N. N. Dremova, L. A. Frolova, K. J. Stevenson, and P. A. A. Troshin, *Energy Fuels*, 2019, **3**, 2627–2632.
24 G. S. Han, Y. H. Song, Y. U. Jin, J. -W. Lee, N. -G. Park, B. K. Kang, J. -K. Lee, I. S. Cho, D. H. Yoon, and H. S. Jung, *ACS Appl. Mater. Interfaces*, 2015, **7**, 23521–23526.
25 A. Agresti, S. Pescetelli, L. Cinà, D. Konios, G. Kakavelakis, E. Kymakis, and A. D. Carlo, *Adv. Funct. Mater*., 2016, **26**, 2686–2694.
26 W. Li, H. Dong, X. Guo, N. Li, J. Li, G. Niu, and L. Wang, *J. Mater. Chem. A*, 2014, **2**, 20105–20111.
27 M. Hadadian, J. -P. Correa-Baena, E. K. Goharshadi, A. Ummadisingu, I. -J. Seo, J. Luo, S. Gholipour, S. M. Zakeeruddin, M. Saliba, A. Abate, M. Grätzel, and A. Hagfeldt, *Adv. Mater*., 2016, **28**, 8681–8686.
28 G. Kakavelakis, E. Kymakis, and K. Petridis, A*dv. Mater. Interfaces*, 2018, **5**, 1800339.
29 N. Alias, A. A. Umar, N. A. A. Malek, K. Liu, X. Li, N. A. Abdullah, M. M. Rosli, M. Y. Abd Rahman, Z. Shi, X. Zhang, H. Zhang, F. Liu, J. Wang, and Y. Zhan, *ACS Appl. Mater. Interfaces*, 2021, **13**, 3051–3061.
30 P. Huang, Z. Wang, Y. Liu, K. Zhang, L. Yuan, Y. Zhou, B. Song, and Y. Li, *ACS Appl. Mater. Interfaces*, 2017, **9**, 25323–25331.
31 D. H. Shin, J. S. Ko, S. K. Kang, and S. -H. Choi, *Appl. Mater. Interfaces*, 2020, **12**, 4586–4593.
32 K. Sobayel, M. Akhtaruzzaman, K. S. Rahman, M. T. Ferdaous, Z. A. A. Mutairi, H. F. Alharbi, N. H. Alharthi, M. R. Karim, S. Hasmady, and N. Amin, *Results Phys*., 2019, **12**, 1097–1103.
33 R. Singh, A. Giri, M. Pal, K. Thiyagarajan, J. Kwak, J. J. Lee, U. Jeong, and K. Cho, *J. Mater. Chem. A*, 2019, **7**, 7151-7158.
34 G. Tang, P. You, Q. Tai, A. Yang, J. Cao, F. Zheng, Z. Zhou, J. Zhao, P. K. L. Chan, and F. Yan, *Adv. Mater*, 2019, 1807689.
35 A. Capasso, F. Matteocci, L. Najafi, M. Prato, J. Buha, L. Cinà, V. Pellegrini, A. D. Carlo, and F. Bonaccorso, *Adv. Energy Mater*., 2016, **6**.
36 Z. Liu, N. Li, C. Su, H. Zhao, L. Xu, Z. Yin, J. Li, and Y. Du, *Nano Energy*, 2018, **50**, 176–181.
37 M. H. Li, T. G. Sun, J. Y. Shao, Y. D. Wang, J. S. Hu, and Y. W. Zhong, *Nano Energy*, 2021, **79**, 105462.
38 Y. Zhou, C. Liu, F. Meng, C. Zhang, G. Wei, L. Gao, and T. Ma, *Sol. RRL*, 2021, 2000713.
39 J. Wang, H. Shi, N. Xu, J. Zhang, Y. Yuan, M. Lei, L. Wang, and P. Wang, *Adv. Funct. Mater*, 2020, **30**, 2002114.
40 H. Liu, X. Fu, W. Fu, B. Zong, L. Huang, H. Bala, S. Wang, Z. Guo, G. Sun, J. Cao, and Z. Zhang, *Org. Electrons.,* 2018, **59**, 253–259.
41 G. Yang, C. Chen, F. Yao, Z. Chen, Q. Zhang, X. Zheng, J. Ma, H. Lei, P. Qin, L. Xiong, W. Ke, G. Li, Y. Yan, and G. Fang, *Adv. Mater*., 2018, **30**, 1706023.
42 N. E. Courtier, J. M. Cave, J. M. Foster, A. B. Walker, and G. Richardson, *Energy Environ. Sci*., 2019, **12**, 1718.
43 Y. Liu, Z. Liu, and E. C. Lee, *ACS Appl. Energy Mater*., 2019, **2**, 1932–1942.
44 G. A. H. Wetzelaer, M. Kuik, M. Lenes, and P. W. M. Blom, *Appl. Phys. Lett*., 2011, **99**, 153506.
45 A. Mahapatra, N. Parikh, P. Kumar, M. Kumar, D. Prochowicz, A. Kalam, M. M. Tavakoli, and P. Yadav, *Molecules*, 2020, **25**, 2299.
46 N. E. Courtier, *Phys. Rev. Appl*., 2020, **14**, 024031–024052.
47 Z. Luo, G. Li, W. Gao, K. Wu, Z. G. Zhang, B. Qiu, H. Bin, L. Xue, F. Liu, Y. Li, and C. Yang, *J. Mater. Chem. A*, 2018, **6**, 6874–6881.
48 J. Troughton, N. Gasparini, and D. Baran, *J. Mater. Chem. A*, 2018, **6**, 21913–21917.
49 L. Xiao, T. Liang, K. Gao, T. Lai, X. Chen, F. Liu, T. P. Russell, F. Huang, X. Peng, and Y. Cao, *ACS Appl. Mater. Interfaces*, 2017, **9**, 29917–29923.
50 H. Jin, E. Debroye, M. Keshavarz, I. G. Scheblykin, M. B. J. Roeffaers, J. Hofkens, and J. A. Steele, *Mater. Horiz*., 2020, **7**, 397–410.
51 I. Zarazua, J. Bisquert, and G. G. Belmonte, *J. Phys. Chem. Lett*., 2016, **7**, 525–528.
52 M. Samiee, S. Konduri, B. Ganapathy, R. Kottokkaran, H. A. Abbas, A. Kitahara, P. Joshi, L. Zhang, M. Noack, and V. Dalal, *Appl. Phys. Lett*., 2014, **105**, 153502.
53 J. A. Carr, M. Elshobaki, and S. Chaudhary, *Appl. Phys. Lett*., 2015, **107**, 203302.
54 N. H. Hemasiri, S. Kazim, and S. Ahmad, *Nano Energy*, **77**, 2020, 105292.
55 M. V. Khenkin, E. A. Katz, A. Abate, G. Bardizza, J. J. Berry, C. Brabec, F. Brunetti, V. Bulovic, Q. Burlingame, A. D. Carlo, R. Cheacharoen, Y. B. Cheng, A. Colsmann, S. Croa, K. Domanski, M. Dusza, C. J. Fell, S. R. Forrest, Y. Galagan, D. D. Girolamo, M. Gratzel, A. Hagfeldt, E. V. Hauff, H. Hoppe, J. Kettle, H. Kobler, M. S. Leite, S. Liu, Y. L. Loo, J. M. Luther, C. Q. Ma, M. Madsen, M. Manceau, M. Matheron, M. McGehee, R. Meitzner, M. K. Nazeeruddin, A. F. Nogueira, C. Odabasi, A. Osherov, N. G. Park, M. O. Reese, F. D. Rossi, M. Saliba, U. S. Schubert, H. J. Snaith, S. D. Stranks, W. Tress, P. A. Troshin, V. Turkovic, S. Veenstra, I. V. Fisher, A. Walsh, T. Watson, H. Xie, R. Yildirim, S. M. Zakeeruddin, K. Zhu, and M. L. Cantu, *Nature Energy*, 2020, **5**, 35-49.
56 M. T. Khan, A. Almohammedi, S. Kazim, and S. Ahmad, *Chem. Rec*., 2019, **20**, 452–465;. M. T. Khan, P. Huang, A. Almohammedi, S. Kazim and S. Ahmad, *iScience*, 2021, **24**, 102024.
57 J. N. Wilson, J. M. Frost, S. K. Wallace, and A. Walsh, APL Mater., 2019, **7**, 010901.